Fuel 181 (2016) 491–502

Contents lists available at ScienceDirect

Fuel

journal homepage: www.elsevier.com/locate/fuel

Full Length Article

Large Eddy Simulation of a 100 kW_{th} swirling oxy-coal furnace

B.M. Franchetti [a], F. Cavallo Marincola [a], S. Navarro-Martinez [a], A.M. Kempf [b,c,*]

[a] Imperial College London, Exhibition Road, SW7 2AZ London, UK
[b] Universität Duisburg-Essen, Chair of Fluid Dynamics, Duisburg 47048, Germany
[c] Center for Computational Sciences and Simulation (CCSS), Universität Duisburg-Essen, Duisburg 47048, Germany

ARTICLE INFO

Article history:
Received 25 July 2015
Received in revised form 20 April 2016
Accepted 5 May 2016
Available online 11 May 2016

Keywords:
Large Eddy Simulation
Coal combustion
Oxy-coal
Turbulent combustion

ABSTRACT

Large Eddy Simulation (LES) has been applied to the swirling 100 kW_{th} OXYCOAL-AC test facility of Aachen University. A set of models to represent devolatilisation, volatile combustion, char combustion and radiation for oxy-coal combustion in an LES framework has been implemented and tested. A qualitative analysis of the flow behaviour and the overall coal combustion processes occurring within the furnace was made. The LES results for the flow field were compared to axial and tangential mean velocity measurements, showing good agreement, particularly in the upstream regions of the flame. The LES results were also compared to oxygen concentrations (vol.) and gas temperature. Overall good agreement was observed in the upstream central regions of the flame, whilst downstream the LES overestimated the combustion rates. It was also found that the recirculation zones are sensitive to char combustion, not just to the rate of devolatilisation as one might expect. An interesting problem occured in the prediction of the velocity profiles, for which the measurements were taken based on coal-particles, so that the outer-most stream remained invisible in the experiments (but not the LES), due to being free from particles. The results show the potential of using LES for more complex oxy-coal combustion burners and opens the way for applications to industrial furnaces.

1. Introduction

Electricity production from coal-fired power plants is expected to keep on playing a dominant role in the future. Carbon Capture and Storage (CCS) can drastically reduce emissions from coal-fired power plants, but leads to lower plant efficiency and increased overall costs. Coal combustion with pure oxygen (O_2) and recirculated exhaust gases facilitates the separation of carbon dioxide (CO_2) from the exhaust gases. The main disadvantages of oxy-coal combustion are the capital costs and the loss in energy efficiency related to the pure O_2 production. Maximising boiler efficiency is thus essential to regain the efficiency lost in the CCS plant, which necessitates an in-depth understanding of the chemical and physical mechanisms involved in oxy-coal combustion.

Experimental measurements inside a Pulverised Coal Combustion (PCC) boiler are difficult and expensive due to poor optical access, making simulations the primary source of detailed information. To date Reynolds-Averaged Navier Stokes (RANS) remains the preferred way for getting in-situ information from within the flame [1–3] as it is relatively cheap. Predictions based on Large Eddy Simulations (LES) promise to be more accurate than RANS, and with the rapid advancement of High Performance Computing have recently gained more attention in the PCC research community. Kurose and Makino [4] performed the first LES of a hypothetical solid fuel flame, where the fuel was modelled as pure methane and the simulation results were presented without any comparison to experimental data. Yamamoto et al. [5] performed a LES of a pre-heated pulverised coal flame. Edge et al. [6] and Gharebaghi et al. [7] carried out the first LES of a 1 MWth scale test facility. Both studies showed that LES can provide more detailed information than a RANS simulation. Recently, Franchetti et al. [8] and Stein et al. [9] presented LES of a pulverised coal jet flame with good agrement with experimental data. In this context Pedel et al. [10] also performed an LES of the pulverised coal jet flame. Their work combined LES with the direct quadrature method of moments (DQMOM) to predict the flame ignition mechanisms. Finally, Rabacal et al. [11] performed a simulation of a large scale laboratory furnace comparing their LES results with experimental measurements of species concentrations (vol.) and temperature. A very exciting project in the context of coal combustion modelling is run at the University of Utah, by Smith, Sutherland and coworkers. They attempt to run the largest combustion LES simulations to

* Corresponding author at: Universität Duisburg-Essen, Faculty of Engineering, Institute of Combustion and Gas Dynamics, Chair of Fluid Dynamics, Carl-Benz-Str. 199, Duisburg 47057, Germany.
E-mail address: andreas.kempf@uni-due.de (A.M. Kempf).

http://dx.doi.org/10.1016/j.fuel.2016.05.015
0016-2361/

date to represent an entire, industrial coal furnace, with very impressive results [http://www.icse.utah.edu, accessed 7.6.2016] and specific work on oxycoal-LES [12].

The combustion of pulverised coal in an O_2/CO_2 atmosphere changes from air combustion due to the different thermo-physical properties of the gas mixture. The density and heat capacity of the gaseous mixture is higher for oxy-PCC due to the higher molecular weight and heat capacity of CO_2 compared to nitrogen (N_2). Moreover, in oxy-PCC, radiative heat transfer will be a priori stronger as CO_2 has higher radiative emission power than N_2. The higher CO_2 concentrations (vol.) in the gas mixture will also affect the char reaction mechanisms.

The purpose of this study is to apply LES to an oxy-coal swirl burner. The 100 kW_{th} OXYCOAL-AC test facility at the Aachen University [13,14] is an ideal test case thanks to the relatively large amount of quantitative experimental data available, and the fact that it is in the heart of the new large-scale research program "Transregio 129 Oxyflame" of Aachen, Bochum and Darmstadt Universities [www.oxyflame.de]. The OXYCOAL-AC burner has been previously modelled in a RANS framework [14,15]. Chen et al. [16] performed a LES with RANS-like symmetry conditions, where they simulated only a section of the burner and then transposed the results to the other sections using periodic boundary conditions, which made the simulations affordable but suppresses some large-scale turbulent modes, and under-predicts the turbulent stresses on the periodic boundaries.

The present simulations were performed using the PsiPhi code, which has been previously used to simulate a laboratory-scale pulverised coal jet flame [8,9] and a large scale laboratory furnace [11]. The present simulation extends our proven modelling approach from previous work to a swirled oxyfuel flame that is likely to become the benchmark for oxyfuel combustion, due to the Aachen flames role in the "Oxyflame" [www.oxyflame.de] project. The results of our simulations permit a first assessment of how well the developed modelling framework can be transferred to oxy-combustion, in a system that is well suited for validation due to its detailed velocity measurements. At the same time, the LES provides valuable insights into the instantaneous velocity, scalar and particle fields and their statistics, which have not been available for this flame before – neither from the experiments or from the RANS simulations.

2. Experimental set-up

A schematic of the furnace and inner quarl is shown in Fig. 1, and a more detailed description is given by Toporov et al. [14]. The furnace is cylindrical with an inner diameter of 0.4 m and a vertical height of 2.1 m. The burner consists of four inlets, where the O_2/CO_2 mixture enters. The coal is injected together with the primary gas stream through an annular orifice. The highly swirled (swirl number 1.2) secondary gas stream is injected through an annulus surrounding the primary stream. For scavenging purposes a tertiary gas stream is injected at very low flow rates. Finally a heated staging gas stream is injected at the outer diameter of the furnace, right at the wall. The purpose of the staging stream is to provide the necessary heat to compensate the higher heat capacity of the gas mixture and to reduce the local stoichiometry of the burner quarl. The flow rates, temperatures and gas compositions of the streams are summarised in Table 1. The furnace is fired with pre-dried Rhenish lignite; its proximate analysis (PA) and ultimate analysis (UA) are shown in Table 2.

The Aachen group [13,14] measured the particle velocity using a Laser Doppler Anemometer (LDA), measuring the velocity of the pulverised coal particles, so that no velocity data is available for the staging stream. Species concentrations (vol.) were measured with a water-cooled suction probe. The gas temperature was obtained using a traversable suction pyrometer. The experimental paper [14] provided data for the particle size distribution, which is composed of 28 classes ranging from 0.9 to 123 μm. The same particle size distribution provided by the experimental paper [14] was retained in the simulations.

3. Numerical modelling

3.1. Gas phase

The simulations were performed using the PsiPhi code, which has been validated extensively for gas combustion [17,18], coal combustion [8,11] and spray combustion [19]. The generalised Favre filtered governing equations were solved for mass, momentum, species mass fraction and enthalpy. In the momentum equation, the viscous stresses were modelled with Smagorinsky's classical turbulent eddy viscosity model [20]. The transported species include: oxygen (O_2), carbon dioxide (CO_2), carbon monoxide (CO), water vapour (H_2O) and the volatile gases (*VG*), modelled as a single postulated substance ($C_aH_bO_c$).

The convective fluxes are approximated using a Central Differencing Scheme for momentum and a Total Variation Diminishing scheme for the scalars. Time integration is performed using a third order explicit low storage Runge–Kutta scheme.

3.2. Solid phase

A Lagrangian approach is used to treat the dispersed phase, which involves tracking the coal particles in time and space. The spray-pdf approach by Jones et al. [21,22] is used, which consists of solving a set of differential equations for the trajectory of the particles and evolution of the particle properties. The position and acceleration of a stochastic particle is obtained from:

$$d\mathbf{x}_p = \mathbf{v}_p dt \tag{1}$$

$$d\mathbf{v}_p = \frac{\tilde{\mathbf{u}}_f - \mathbf{v}_p}{\tau_p} dt + \sqrt{C_o \frac{k_{sgs}}{\tau_t}} d\mathbf{W} \tag{2}$$

where $\mathbf{v}_p$ and $\tilde{\mathbf{u}}_f$ are the particle and filtered gas velocity respectively, and $\tau_p^{-1} = 3/4(\bar{\rho}_g C_D)/(\rho_p d_p)|\tilde{\mathbf{u}}_f - \mathbf{v}_p|$ is the particle relaxation time. The drag coefficient C_D is evaluated using the Yuen-Chen empirical relationship [23]. The first term on the right hand side (RHS) of Eq. (2) represents the influence of the resolved scales of the carrier gas on the particles. The second term represents the influence of the sub-grid scales on the particle motion. The dispersion constant C_o is set to unity [22]. The timescale $\tau_t = \tau_p\left(\tau_p k_{sgs}^{1/2}/\Delta\right)^{0.6}$ represents the rate of interaction between the particle and gas-phase turbulence and $k_{sgs} = 2\Delta^2 C_s^{2/3}\widetilde{S}_{ij}\widetilde{S}_{ij}$ is the unresolved kinetic energy of the gas phase, which can be obtained by an equilibrium assumption for the sub grid turbulence [21,22,24], where $\widetilde{S}_{ij}$ is the strain rate tensor. Finally, $d\mathbf{W}$ represents the incremental Wiener process.

The rate of change of temperature of a particle is determined from:

$$\frac{dT_p}{dt} = \frac{Nu}{3Pr}\frac{c_{p,f}}{c_{p,p}}\left(\frac{T_g - T_p}{\tau_m}\right) - \frac{\dot{m}_{vg}}{m_p}\frac{h_{dev}}{c_{p,p}} + \frac{\dot{Q}_{char}}{m_p c_{p,p}} + \frac{\dot{Q}_{rad}}{m_p c_{p,p}} \tag{3}$$

The first term on the RHS of Eq. (3) represents the heat exchange with the gas phase due to convection and conduction, where $c_{p,f}$ is the specific heat of the gas mixture and $c_{p,p}$ = 1100 J/kg K is the

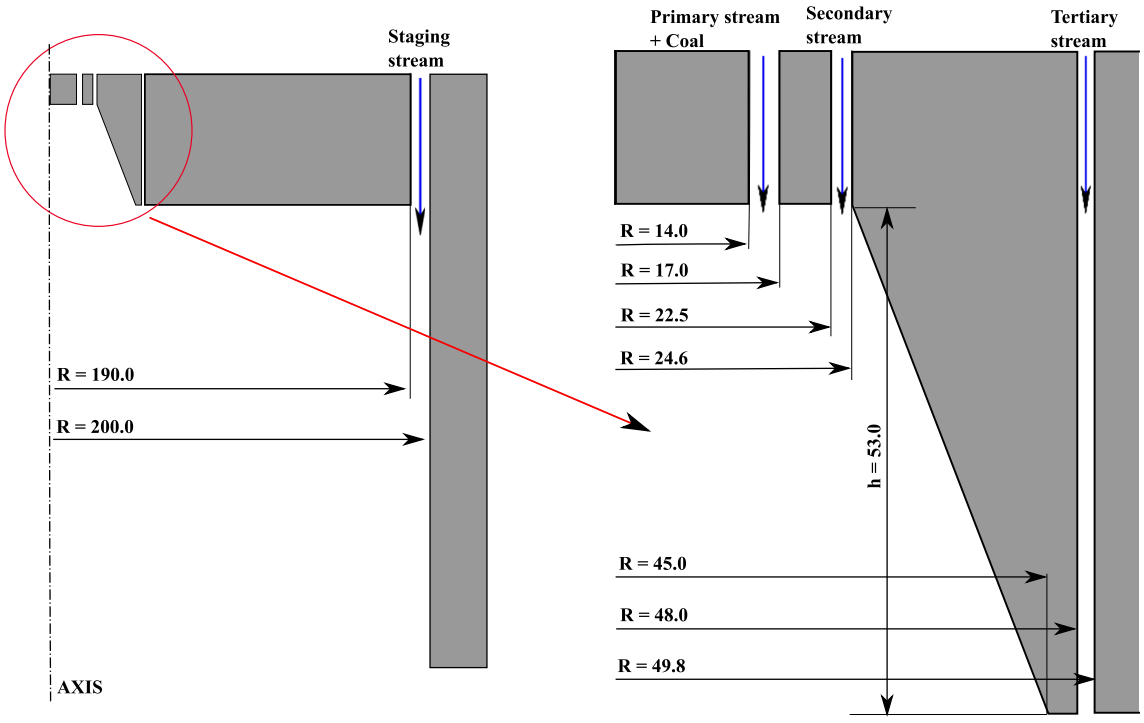

Fig. 1. Schematic of the upper section of the Aachen pulverised coal furnace. Dimensions are not to scale, units in mm.

Table 1
Experimental conditions [14].

	$\dot{m}$ (kg/h)	O_2 (vol%)	CO_2 (vol%)	T (°C)
Coal	6.5	–	–	–
Primary	17.6	0.19	0.81	40
Secondary	26.6	0.21	0.79	60
Tertiary	1.5	0.21	0.79	60
Staging	54.9	0.21	0.79	900

Table 2
Rhenish lignite PA and UA [14].

PA	(wt%)	UA	(wt%)
Moisture	8.40	C	77.03
Ash	4.10	H	4.85
Volatile matter	46.60	N	16.60
Fixed carbon	40.90	O	0.98

specific heat of the coal particle, which was assumed constant for this work. The Prandtl number Pr was set to 0.6, Nu denotes the Nusselt number calculated by the Ranz–Marshall correlation [25], and $\tau_m = \rho_p d_p^2/(18\mu_g)$ is the diffusion relaxation time. The second term represents the heat loss due to the volatiles being released from the particle, where h_{dev} is the latent heat of evaporation of the volatiles. The first two terms on the RHS of Eq. (3) are based on the heat transfer equation of a liquid spray [24]. Finally, $\dot{Q}_{char}$ represents the heat exchange between the gas and particle due to char combustion, and $\dot{Q}_{rad}$ represents the heat exchange of the particle due to radiation, as explained in Section 3.6.

3.3. Two way coupling terms

A source term $\bar{\bar{S}} = 1/\Delta^3 \Sigma_{i=1}^{P} S^p$ accounts for the contribution of the dispersed phase on the gas phase in each computational cell, where P is the number of particles present in a cell's volume and S^p is the source term arising from the pth particle. Each coal particle is assumed to be composed of volatile matter, char and ash. Ash acts as an inert substance, and the change in mass of the pth particle is related to the yield of the volatile gases (dm_{vg}/dt) and char burning rate (dm_{char}/dt), such that:

$$\frac{dm_p}{dt} = \frac{dm_{vg}}{dt} + \frac{dm_{char}}{dt} \tag{4}$$

The effects of particle momentum exchange with the continuous phase have been studied [26] and were found to have a negligible influence due to the low particle concentration; consequently they have been ignored in this study. Finally, the enthalpy change of the gas phase due to the coal particles burning is given by:

$$\dot{S}_{p,h} = -\dot{Q}_{con} - \dot{Q}_{rad} + \frac{dm_p}{dt} h(T_p)_{vap} - \frac{dm_p}{dt}[h_s(T_g)_{vap} + h_s(T_p)_{vap}] \tag{5}$$

The first term on the RHS of Eq. (5) accounts for the convective effect of the coal particle on the surrounding gas, which can be obtained from the first term on the RHS of Eq. (3), and the second term accounts for the radiative effects. The third term is responsible for the enthalpy increase due to the added mass in the gas phase from the coal particle at the particle temperature. The fourth term represents the energy required to bring the sensible enthalpy of the released gases $(h_{s,vap})$ from the particle temperature to the gas temperature.

3.4. Coal combustion model

Previous studies [27,28] found that the exchange of N_2 for CO_2 in oxyfuel combustion does not have much influence on devolatilisation. It was thus deemed sufficient for the purpose of this study to represent the devolatilisation of the volatile gases from the coal particle using the single-step reaction rate model [29], which assumes a single reaction for the total weight loss of the volatiles:

$$\frac{dm_{vg}}{dt} = k_v(VM - VG) \tag{6}$$

$$k_v = A_v T_p^{\beta} \exp\left(-\frac{E_v}{\mathbb{R}T_p}\right) \tag{7}$$

The constants A_v, E_v and β follow a modified Arrhenius expression, VG is the total mass of volatile gases that have left a coal particle and VM is the initial mass of volatile matter inside the coal particle adjusted by a factor $Q = VM_{CPD}/VM_{PA}$ to account for the higher yield of volatile gases at higher temperatures [29]. The values used were $Q = 1.15$ and the single rate parameters $A_v = 4.727 \times 10^9$ (1/s), $E_v = 10.256 \times 10^3$ J/(kmol K) and $\beta = -0.9503$ were obtained from a fit of the Chemical Percolation Devolatilisation (CPD) Model [30]. The input values for the CPD model were obtained from the proximate and ultimate analysis through the correlation of Genetti et al. [31].

Char combustion in a CO_2 enriched environment can differ considerably compared to combustion in air. The char burning temperatures and residence times are lower in a O_2/CO_2 environment compared to a O_2/N_2 environment [28]. This difference can be attributed to the char-CO_2 and char-H_2O gasification reactions. Three heterogeneous reactions were considered in the present work:

$$C_{char} + 0.5O_2 \rightarrow CO \tag{8}$$

$$C_{char} + CO_2 \rightarrow 2CO \tag{9}$$

$$C_{char} + H_2O \rightarrow CO + H_2 \tag{10}$$

The reaction rates of Eqs. (8)–(10) are obtained from the Baum and Street model [32]:

$$\frac{dm_{char}}{dt} = A_p p_{ox}\left(\frac{1}{R_c} + \frac{1}{D_o}\right) \tag{11}$$

Here, $D_o = C_{diff}/d_p[(T_p + T_g)/2]^{3/4}$ is the diffusion rate term. The chemical reaction rate term is obtained via the Arrhenius expression $R_c = A_c \exp(-E_c/\mathbb{R}T_p)$. The diffusivity constants and Arrhenius coefficients for the reactions (8)–(10) were provided by Toporov et al. [14] and are consistent with their RANS simulations, and are reproduced in Table 3.

3.5. Gas phase turbulent combustion

The volatile gases were modelled as a single postulated substance $C_aH_bO_cN_d$ ($a = 2.58$, $b = 3.98$, $c = 0.87$, $d = 0$). The enthalpy of formation of the volatile gases was determined to be $h_{f,vol} = -587.86$ MJ/kmol. The homogeneous chemistry was described by a two-step mechanism:

$$C_{2.58}H_{3.98}O_{0.87} + 1.85O_2 \rightarrow 2.58CO + 1.99H_2O \tag{12}$$

$$CO + \frac{1}{2}O_2 \rightarrow CO_2 \tag{13}$$

The reaction rate $\tilde{w}_{vg}$ was modelled using the Eddy Break Up (EBU) [35] model adjusted for LES [36].

$$\tilde{w}_{vg} = c_{EBU}\bar{\rho}|\widetilde{S}| \min\left(\widetilde{Y}_{fu}, \frac{\widetilde{Y}_{ox}}{s}, c_2\frac{\widetilde{Y}_{pr}}{1+s}\right) \tag{14}$$

The model constants are $c_{EBU} = 4.0$ and $c_2 = 0.5$, while s is the stoichiometric coefficient. Ideally the volatile gases should be modelled as an ensemble of multiple species, however this would require a very large reaction mechanism, resulting in a considerable increase in computational cost, which would be unfeasible for the already very expensive simulation (see Table 4). Moreover, using a large mechanism for this flame would require dedicated sub-grid modelling of turbulence-chemistry interaction which is done by the EBU model but not with a direct application of the mechanism.

3.6. Radiative heat transfer

The Radiative Transfer Equation (RTE) is solved using the Discrete Ordinates Method (DOM) [37–39]. In the DOM, the RTE is discretised and solved for n different direction $\hat{s}$, and summed over all directions in the integral (4π). In this work the RTE was discretized and solved for 24 directions using the S_4 approximation. The total incident radiation G is calculated from the sum of all the intensities impinging on a given control volume:

$$G = \int_{4\pi} I(\hat{s})d\Omega \approx \sum_{i=1}^{n} w_i I_i \tag{15}$$

where w_i is the quadrature weight associated for each direction.

The spectral properties of the participating media were treated with a grey gas model. Gosman and Lockwood [40] found that in the context of coal combustion CO_2, H_2O and the volatile gases have a dominant impact over other gaseous species. In this work the volatile gases are treated as a single postulated substance $C_aH_bO_c$ and the gas absorption co-efficient was determined using an empirical relationship [40]:

$$\kappa_g = 0.2X_{vg} + 0.1(X_{CO_2} + X_{H_2O}) \tag{16}$$

The heat exchange of a particle with the gas phase due to radiation $\dot{Q}_{rad}$ (Eq. (5)) can be obtained by:

$$\dot{Q}_{rad} = 1/4\epsilon_p \pi d_p^2 (4\pi I_{b,p} - G) \tag{17}$$

The particle's absorption coefficients κ_p and scattering coefficient σ_p in a given cell are determined according Chui et al. [41]:

$$\kappa_p = \epsilon_p \sum_i N_i \frac{\pi d_{p,i}^2}{4} \tag{18}$$

$$\sigma_p = (1 - \epsilon_p)\sum_i N_i \frac{\pi d_{p,i}^2}{4} \tag{19}$$

where N_i is the particle number density relevant to the size class d_i, and ϵ_p is the particle emissivity which depends on the char-burnout, and the proportions of volatile content and ash found in

Table 3
Rate parameters and diffusion coefficients for the oxy-char surface reactions [14].

Reaction	n	A_c	E_c	Temp (°C)	C_{diff}	Ref.
(8)	1	0.005	174,000	>677	4.41×10^{-12}	[14,33]
(9)	1	0.135×10^{-3}	135,500	850–950	2.47×10^{-12}	[14,34]
	1	6.35×10^{-3}	162,000	>950		
(10)	1	0.319	208,000	860–960	2.47×10^{-12}	[14,34]
	1	1.92×10^{-3}	147,000	>960		

Table 4
Simulation computational costs.

	Coarse grid $\Delta = 2$ mm	Fine grid $\Delta = 1$ mm
No of cells	16 M	128 M
No of CPUs	96	384
Time steps	100,000	170,000
Accumulation time	3.25 s	3.00 s
Days (without rad.)	8	27
CPU hours (without rad.)	18,000	250,000
Days (with rad.)	15	NA
CPU hours (with rad.)	35,000	NA

the particle. Finally, the particle blackbody intensity $I_{b,p}$ is obtained via:

$$\kappa_p I_{b,p} = \epsilon_p \sum_i N_i \frac{\pi d_{p,i}^2}{4} \frac{\sigma T_{p,i}^2}{\pi} \tag{20}$$

3.7. Simulation

The furnace geometry was described by a Cartesian mesh of $0.4 \times 0.4 \times 0.8\ m^3$ in size, which represents a reduced domain length compared to the whole furnace length (2.1 m). Coarse and fine grid simulations were performed with equally sized cubic cells (Δ = 2 mm and Δ = 1 mm), leading to 16M and 128M cells respectively. The coarse grid simulations were all performed on 96 processors and took approximately 15 days (≈35,000 CPU hours) for 100,000 steps. Without radiation, the equivalent simulation took approximately half of the time. The fine grid simulation was performed on 384 processors and was only performed without radiation, as the coarse grid simulation showed the effect of radiation to be small as explained in more detail in Section 5.1. The fine grid simulations took approximately 27 days (≈250,000 CPU hours) to perform 170,000 iterations, which were necessary to achieve a converged solution. A summary of the computational cost of the fine and coarse grid simulations is shown in Table 4.

At the inlets, top hat velocity profiles were imposed, corresponding to the nominal volume fluxes. Pseudo-turbulent inflow conditions were generated [42] with an inlet fluctuation $u' = 0.5$ m/s and a length scale L_{turb} = 3 mm. Laminar flow conditions were assumed for the staging stream. Immersed boundaries were set at the burner walls. For radiation, the boundary conditions were taken from Toporov et al. [14], who provided temperature and emissivity values for the furnace and burner of 1000 °C (ϵ = 0.7) and 300 °C (ϵ = 0.2) respectively. For the open boundaries at the inflow and outflow of the domain, blackbody conditions were assumed (ϵ = 1.0). Approximately 11 million computational particles per second were fed into the domain, where each computational particle represents an ensemble of ten real particles. Approximately 1.8 million particles were present in the domain at a given time during the simulation. The particle size distribution given by Toporov et al. [14] was used in the simulations.

4. Results

4.1. Flow field

Fig. 2 shows the volume rendered particle positions across the whole domain. The highest particle density is found in the burner quarl, where the particles are fed in from the inlet. The particle cloud expands axially and radially almost uniformally. Upstream (z < 0.2 m) very few particles are found close to the walls as the incoming staging stream pushes the particles towards the center of the domain.

Fig. 3 shows the grey scale renderings of the instantaneous mean axial and tangential gas velocities. The coal carrying primary stream and the swirling secondary stream merge together almost immediately, and form a single stream that expands radially outwards and starts to decay at approximately z = 0.1 m downstream from the burner outlet. The swirling secondary stream and the quarl geometry are responsible for the very strong internal recirculation zone (IRZ) which is clearly visible inside the quarl.

Fig. 4 shows the mean axial (a) and tangential (b) velocity profiles predicted by the LES, and compared to experimental measurements at four axial locations from the burner outlet. Fig. 4(a) shows that the LES correctly predicts the magnitude and size of the axial velocity maximum and tangential velocity minimum at z = 0.025 m and z = 0.05 m. Another axial velocity peak is observed close to the furnace walls, caused by the staging stream.

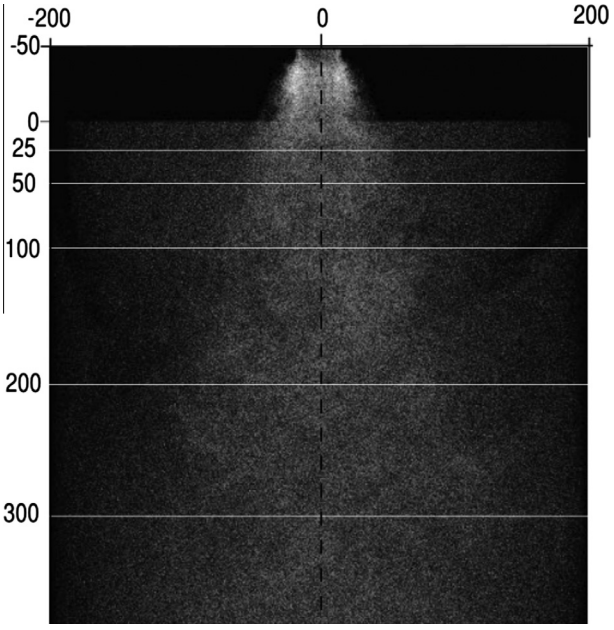

Fig. 2. Volume rendering of individual particle positions from the fine grid LES, bright regions show a high particle density (dimensions in mm).

A strong internal recirculation zone (IRZ) is clearly visible inside the quarl in Fig. 1. The experimentalists measure a strong backward axial velocity ≈−3 m/s at the two upstream planes, z = 0.025 m and z = 0.05 m, which is correctly captured by the LES. At z = 0.2 m, the experiments show a slower (≈−1 m/s) but much larger external recirculation zone (ERZ), which extends from r = 0.1 m to the furnace wall. The ERZ predicted by the LES is smaller in size and magnitude. Moreover the LES over-predicts the velocity profiles at z = 0.3 m. The discrepancies between the LES results and the experimental measurements in the downstream planes can be attributed to uncertainties in the staging stream. The behaviour of the staging stream is of crucial importance for this burner given that it transports more than 50% of the fluid mass into the domain. However, the experiments used the coal particles in the flow for the LDA measurements, which (see Fig. 2) will be mostly present upstream, in the central region of the furnace. Consequently the added mass (and velocity) provided by the staging stream will not be captured by the LDA measurements, turning the staging air into an "invisible" mass flow. To analyse the effect of the staging stream, a coarse adjustment to the LES results was made. The volume flow of the staging stream was subtracted throughout the domain width at the z = 0.3 m plane and throughout half of the domain width (r > 0.1 m) for the z = 0.2 m plane. In Fig. 4(a) the LES results are closer to the experimental measurements when the staging air flow is subtracted from the experimental data. A real compensation of the experimental uncertainty introduced by the "invisible" staging air cannot be reproduced by LES-statistics of particle velocity, since it is not clear how large the particle concentration needs to be for the experiment to get a valid signal (one should note that the axial velocity and the local concentration (vol.) of gas from the staging stream are likely to be correlated).

Fig. 5 shows the ratio between turbulent viscosity and laminar viscosity (μ_τ/μ_l) for the fine grid simulation. Regions of intense turbulence can be observed in the corner between the quarl and the inlet plane. It should be noted that in this small region, the viscosity ratio reaches higher values (≈40) than what is normally

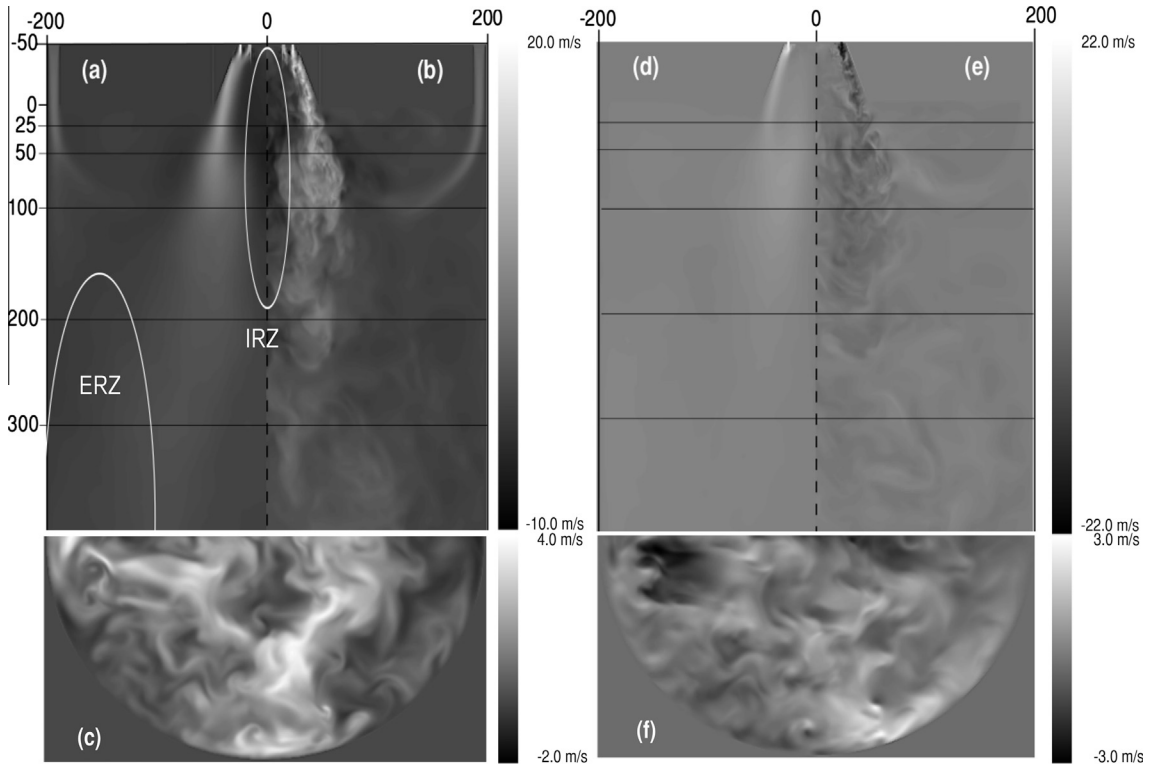

Fig. 3. Fine grid LES grey scale renderings of axial (left) and tangential (right) gas velocities in a cross-sectional plane along the central axis (a and d) mean, (b and e) instantaneous and (c and f) instantaneous cross section at $z = 0.35$ m. The regions IRZ and ERZ indicate the inner and external recirculation zones (dimensions in mm).

aimed for (≈20) [43] in the high-quality LES of laboratory scale gas burners, indicating that achieving a good grid resolution of swirled coal burners is still not an easy feat.

4.2. Devolatilisation and volatile combustion

Fig. 6 shows the mean volatile yield and instantaneous volatile gas concentration (vol.) in a cutting plane through the central axis of the burner. The volatile yield represents the amount of volatiles being released by the pulverised coal particles at a given time step, based on the single step devolatilisation model Eq. (6). The volatile gases are released rapidly, close to the burner inlet in the quarl and are mostly consumed in the central upstream region of the flame $z < 0.1$ m.

Fig. 7 shows the grey scale renderings of the mean (a) and instantaneous (b) O_2 concentrations (vol.) in the furnace in a cutting plane through the central axis of the burner. The oxygen enters the quarl through the primary and secondary stream and is transported radially outwards, carrying the coal particles along. Most of the oxygen from the primary and secondary stream, together with the coal particles, are carried into the highly swirling flow surrounding the IRZ, and the particles start heating up very rapidly, thereby releasing rapidly the volatile gases (see Fig. 6(a)). Once the volatile gases are released in the vortex surrounding the IRZ, they burn fast, limited only by the rate of mixing according to the EBU model. In fact, the volatile combustion process only occurs in the vortex surrounding the IRZ but hardly within the IRZ itself. In the vortex surrounding the IRZ most of the combustion occurring will relate to the burning of the volatile gases to form CO via reaction (12). This is observable in Fig. 8, which shows a high CO concentration (vol.) in the IRZ region. Within the IRZ itself, there is no oxygen left (see Fig. 7) to burn the remaining CO and volatile gases, which causes parts of the unburned volatile gases and CO to be transported back into the quarl.

Fig. 7(d) shows the H_2O, volatile gases (*VG*) and O_2 mole fraction profiles obtained from the LES and the experimental measurements of O_2 concentration (vol.) at four axial distances from the burner outlet. Both the experiments and the LES show very low O_2 concentrations (vol.) at $z < 0.2$ m in the central region of the furnace. In the same region, the LES results show diminishing *VG* and increasing H_2O concentrations (vol.), which confirms that intense volatile combustion must be occurring there. For all of the upstream planes the O_2 levels predicted by the LES follow the experimental measurements reasonably well between $0 < r < 0.05$ m, indicating that the volatile combustion process is being captured satisfactorily by the LES. Nonetheless, in the region between $0.05 < r < 0.15$ m the LES over-estimates the O_2 concentration. This can be attributed to the devolatilisation and EBU models, which might over-estimate the volatile release rate and their combustion rate. If the volatile gases are present outside the IRZ they can burn with the surrounding O_2, lowering its concentration (vol.) between $0.05 < r < 0.15$ m. A second reason for the deviations might be related to the devolatilisation model and will be discussed in Section 5.

4.3. Char combustion

More than half of the O_2 entering the furnace comes from the staging stream, which drives most of the char combustion process, especially downstream. The O_2 in the staging stream flows inwards towards the centre of the furnace filling both the upstream outer region of the furnace and downstream throughout the furnace width. After all the volatile gases have been released, the char particles that escape the IRZ surrounding vortex are transported axially and radially outwards and start reacting with the O_2 from the staging stream. Fig. 8 shows that the bulk of the char combustion occurs outside IRZ, and that several small regions of high instantaneous CO concentration (vol.) surround the IRZ. These

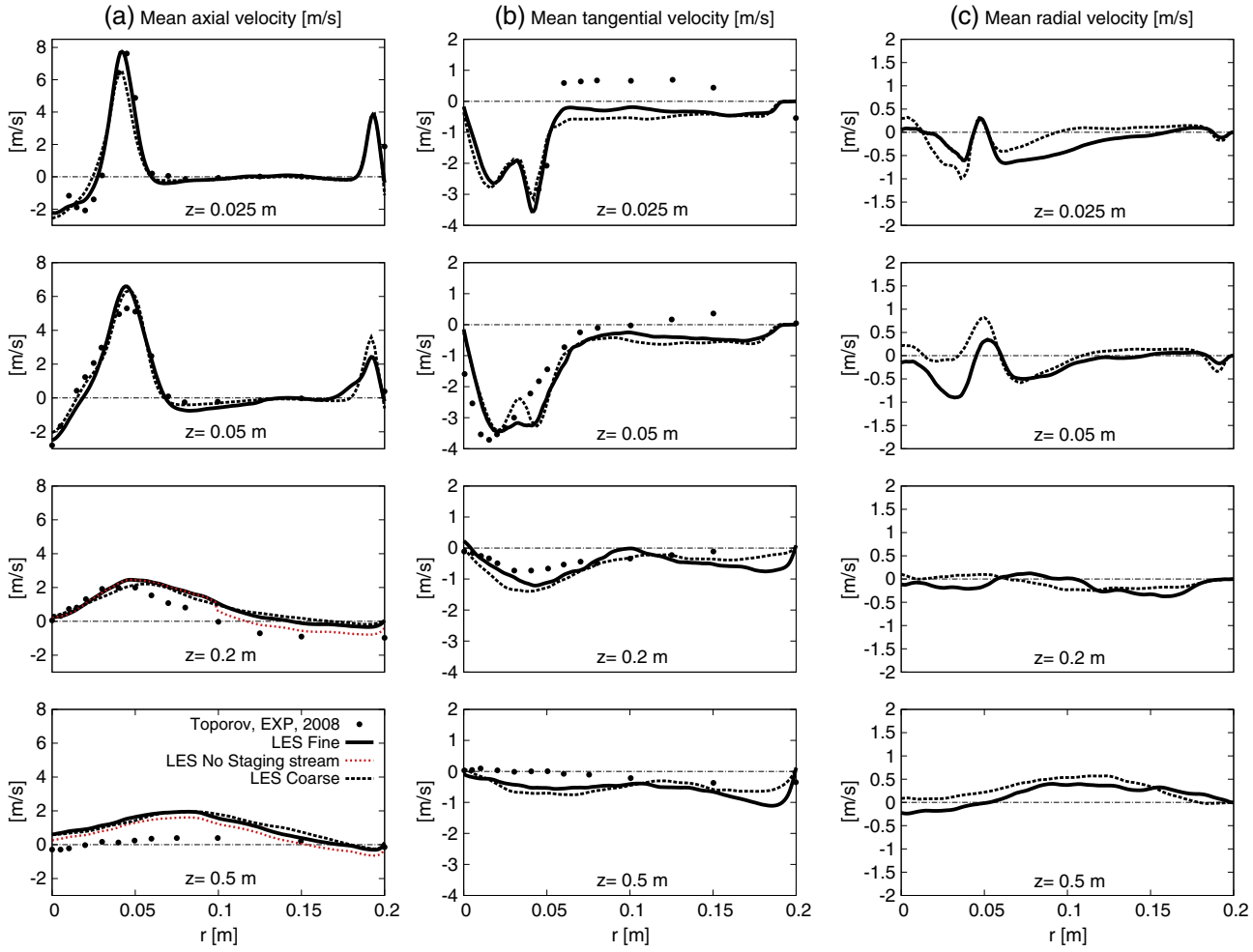

Fig. 4. Comparison between LES fine (Δ = 1 mm) (solid line) and coarse (Δ = 2 mm) (dotted line) (a) mean axial and (b) tangential gas velocity profiles with experimental measurements. (c) Mean radial gas velocity profiles, radial profiles were not available from the experiments.

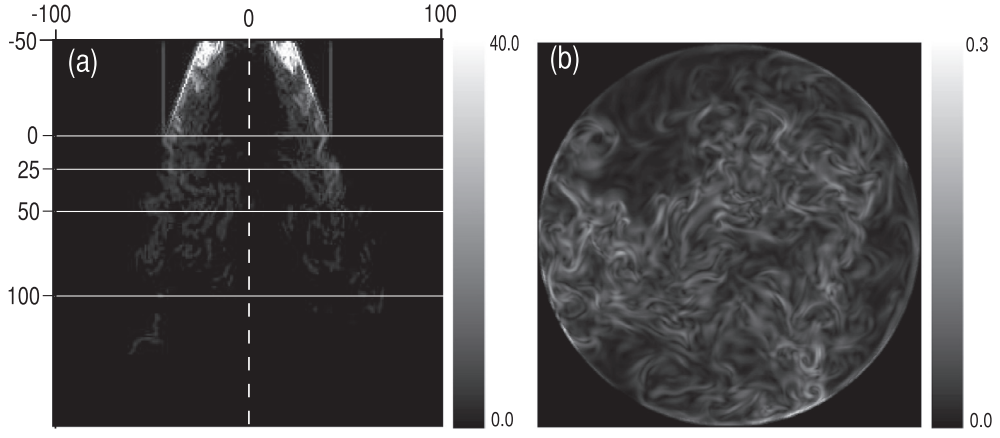

Fig. 5. Fine grid instantaneous LES grey scale renderings of the viscosity ratio μ_τ/μ_l in (a) cutting plane through the central axis and (b) cross section at z = 0.35 m (dimensions in mm).

are due to local regions of intense char combustion, where CO is primarily produced by char combustion according to Eqs. (8) and (9). Fig. 9 compares the mean values of the char-O_2 reaction and the char-CO_2 reaction along the central plane of the furnace. The char-O_2 reaction rate contributes about an order of magnitude more than the char-CO_2 gasification to the total char combustion rate. The exact contributions of the char-O_2 and char-CO_2 reactions to char consumption are 92.91% and 7.00% respectively, which is very close to the values observed by Chen et al. [16], who predicted 91.90% and 7.46% and only 0.68% for the char-H_2O reaction. As the contribution of the char-H_2 reaction was found by Chen et al. [16] to be <1% it was ignored in the present calculations to avoid the need for transporting H_2. For the present test case the char oxidation reaction is particularly dominant due to the relatively low

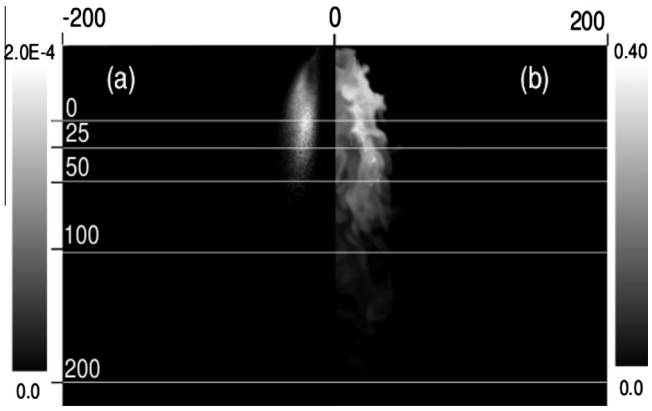

Fig. 6. Fine grid LES results showing (a) the time averaged volatile yield (kg/m^3) and (b) instantaneous volatile gas concentrations (vol.) in a cutting plane through the central axis (dimensions in mm).

temperatures throughout the domain (see Fig. 10), which does not necessarily imply that such is the case for every oxy-coal combustion process. The char-CO_2 gasification process may become important in regions of high temperatures and low O_2 concentration. As shown in Fig. 9, within the central region of the flame, some char-CO_2 gasification is observed even in the absence of O_2, which may contribute considerably to the overall combustion process.

Most of the volatile gases leave the coal particles in the vortex surrounding the IRZ, and the devolatilisation process terminates close to the burner inlet. Fig. 9 shows that most of the char combustion occurs in the region of $z < 0.3$ m and that little char is burnt downstream of $z > 0.3$ m. This provides additional justification for simulating the boiler only to 0.8 m downstream from the burner, excluding the regions even further downstream.

4.4. Temperature

Fig. 10 shows the grey scale renderings of the mean (a) and instantaneous (b) gas temperature in the furnace in a cross-sectional plane along the central axis and (c) an instantaneous cross-sectional image of the gas temperature at $z = 0.35$ m. The combustion of the volatiles results in the rapid temperature increase in the location of the primary/secondary stream jet in Fig. 10. The temperature is highest at this point within the quarl, reaching values of approximately ≈1400 K. At the centre of the quarl the temperature is lower ≈1000 K, which confirms that limited combustion is occurring there and the temperature rise is mainly due to the recirculating hot products (see Section 4.2). The combustion of the volatiles extends to $z \approx 0.2$ m, contributing to the rapid temperature rise occurring in the centre of the furnace between $z = 0.05$ m and $z = 0.2$ m. In the downstream region of the furnace ($z > 0.3$ m), overall high temperatures are observed everywhere along the central axis of the flame, Fig. 10(a and b), and throughout the furnace cross-section, Fig. 10(c). The temperature rise is a result of the CO produced by the char combustion burning with the oxygen from the staging stream. In Fig. 10(d) the gas temperature profiles predicted by the LES are compared to experimental measurements at four axial locations from the burner outlet. At the $z = 0.05$, 0.1 and 0.2 m planes, a good agreement is observed

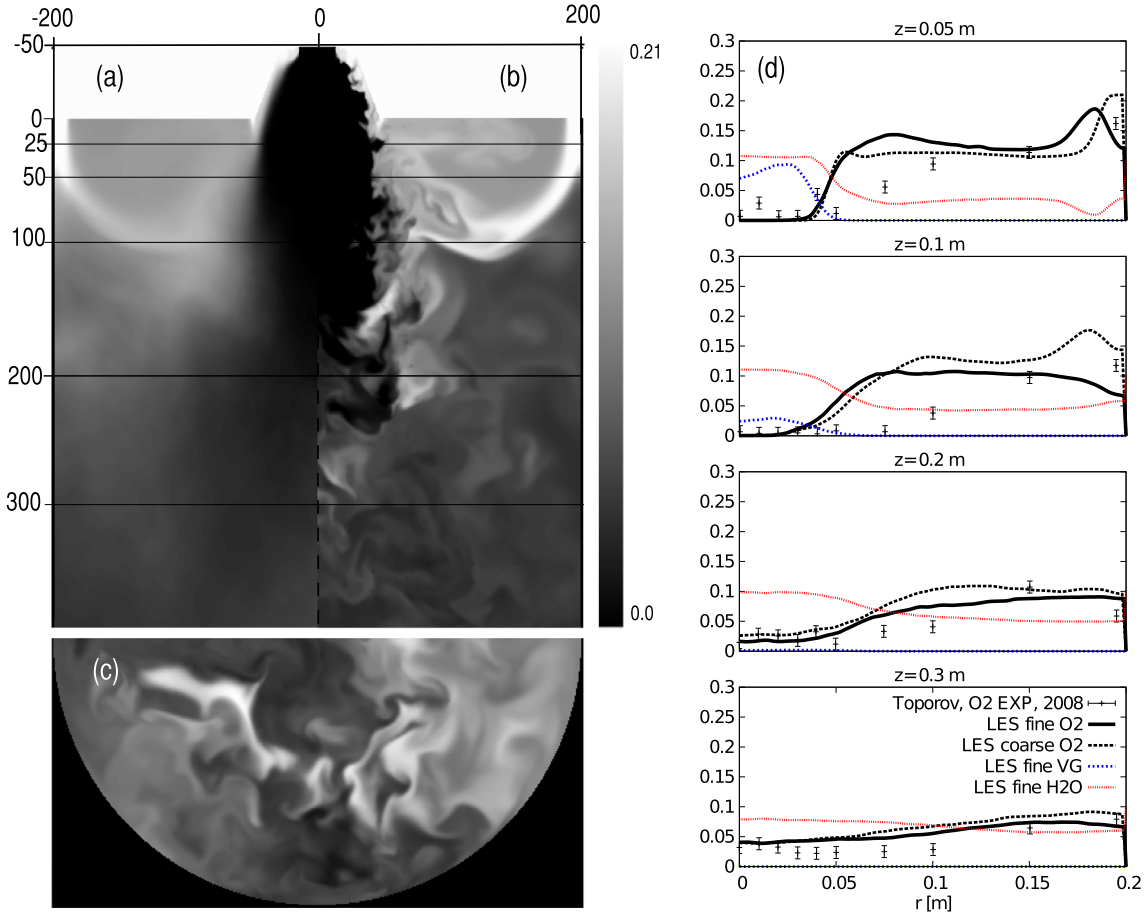

Fig. 7. *Left*: Fine grid LES grey scale renderings of O_2 concentration (vol.) in a cutting plane through the central axis (a) mean, (b) instantaneous and (c) instantaneous cross section at $z = 0.35$ m (dimensions are in mm). *Right* (d): Fine O_2, *VG* and H_2O and coarse O_2 concentrations (vol.) predicted by LES and O_2 experimental measurements.

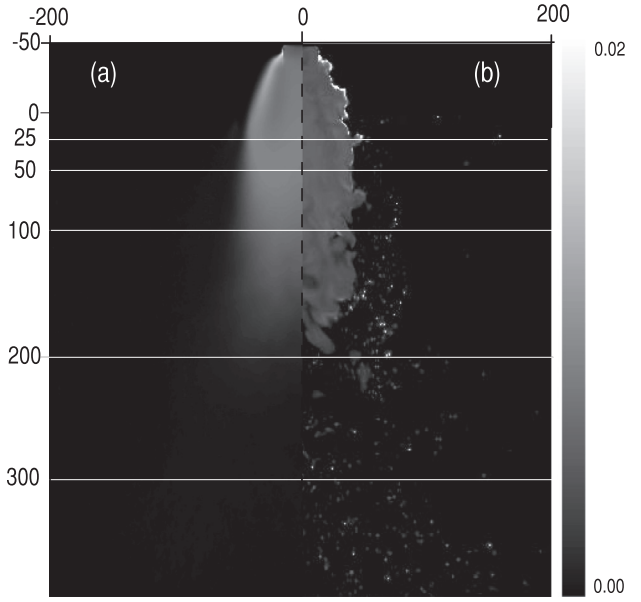

Fig. 8. Fine grid LES (a) mean and (b) instantaneous grey scale renderings of CO concentration (vol.) in a cross-sectional plane along the central axis (dimensions in mm).

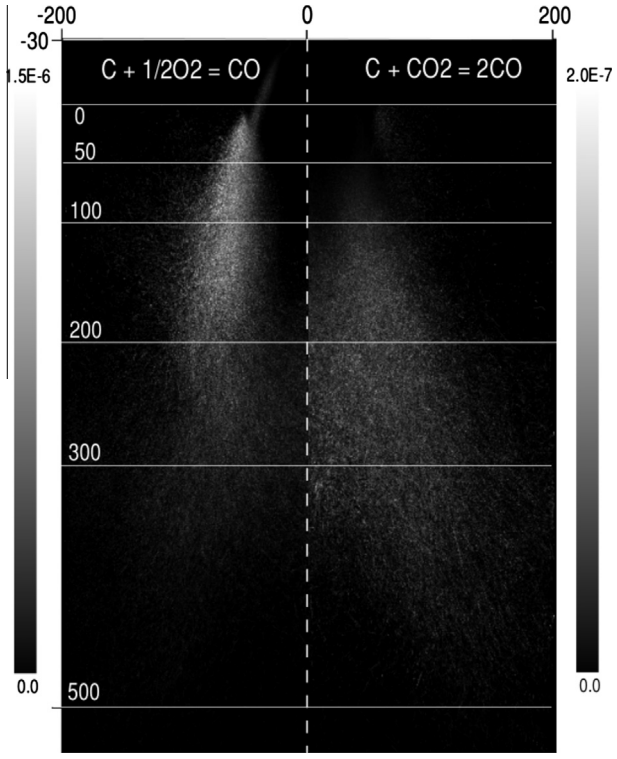

Fig. 9. *Left*: Grey scale rendering of the mean char-O_2 and char-CO_2 reaction at a given time-step in a cross-sectional plane along the central axis (kg/m^3). *Right*: Char-CO_2 reaction mainly occurs where char-O_2 reaction has ceased (dimension in mm).

between the LES and experiments. At the $z = 0.3$ m plane, the LES overestimates the experimental measurements by up to 200 K. The high temperatures predicted by the LES cause an over-expansion of the gases, which could explain the discrepancy in axial velocity at the $z = 0.3$ m plane in Fig. 4. An attempt to understand the discrepancies in the downstream temperatures between the LES and experiments is made in the next section.

5. Parametric study

A parametric study has been performed, to understand what affects the results and which models must be improved to enhance the predictions.

The effect of grid refinement on the simulation results was assessed by performing two grid simulations with cell size $\Delta = 1$ mm and $\Delta = 2$ mm. Figs. 4, 7 and 10 compare the fine and coarse grid simulation results for the velocity, temperature and oxygen concentration. The oxygen concentration (vol.) predicted by the fine grid simulation follows more closely the experimental data. For the fine grid simulations, the better description of mixing meant that the EBU model can provide a better description of the reaction rates. However, for the downstream planes the temperature results of the coarse and fine grid simulations are almost identical. This suggests that the downstream temperature discrepancies are not related to the gas combustion rates but to processes independent of mixing such as char combustion or radiation. The results between the two simulations did not differ considerably, and therefore in all further simulations for the parametric study, the coarse grid was retained.

5.1. Effect of radiation

Fig. 10(d) shows the gas temperature profiles for the coarse grid LES with and without radiation (dotted lines). The temperature at the furnace walls were set to 1000 °C as suggested by Toporov et al. [13,14], which is slightly colder than the upstream temperature measurements close to the walls. The upstream gases close to the furnace walls thus lose heat, which results in the slight drop in temperature observed at the $z = 0.05$ m plane and close to the walls at the $z = 0.1$ m plane. Throughout the central region of the flame, radiation has a negligible impact. In this region the walls are too far (and not cold or hot enough) to have a considerable impact. Moreover, the transporting medium temperature is not very hot, which limits the amount of radiative heat dispersed to either the surroundings or transferred to the dispersed phase.

The current results are unable to assess alone whether radiative effects are really negligible within the central regions of the flame. Consequently, it is possible that the discrepancy in temperature observed at $z = 0.3$ m may also be a result of the radiation model. Treating the radiative properties of the participating medium as grey is somewhat simplistic. A more advanced treatment of the radiative properties would be to use the Weighted Sum of Grey Gas (WSGG) method, where the radiative properties of the medium are represented by a number (usually four or five) grey gases, and where the RTE is solved for each grey gas, having its own absorption coefficient and weight, rather than a single value to represent the whole mixture. Cavallo Marincola [44] compared both the grey gas and WSGG approaches for the IFRF No. 1 burner [45] and found that the grey medium assumption overestimated the temperatures downstream, whilst the WSGG approach gave overall better results. The WSGG method however, leads to a considerable increase in computational times.

Moreover, Toporov et al. [13,14] provided the radiation boundary conditions that were used in this work. A more thorough analysis of the radiative properties at the burner walls could show that more appropriate radiative boundary conditions are required for the burner, possibly resulting in a bigger impact on the temperature predictions.

5.2. Char combustion

Fig. 11 compares the temperature and oxygen concentration (vol.) results for two LES, where in one the char combustion rate

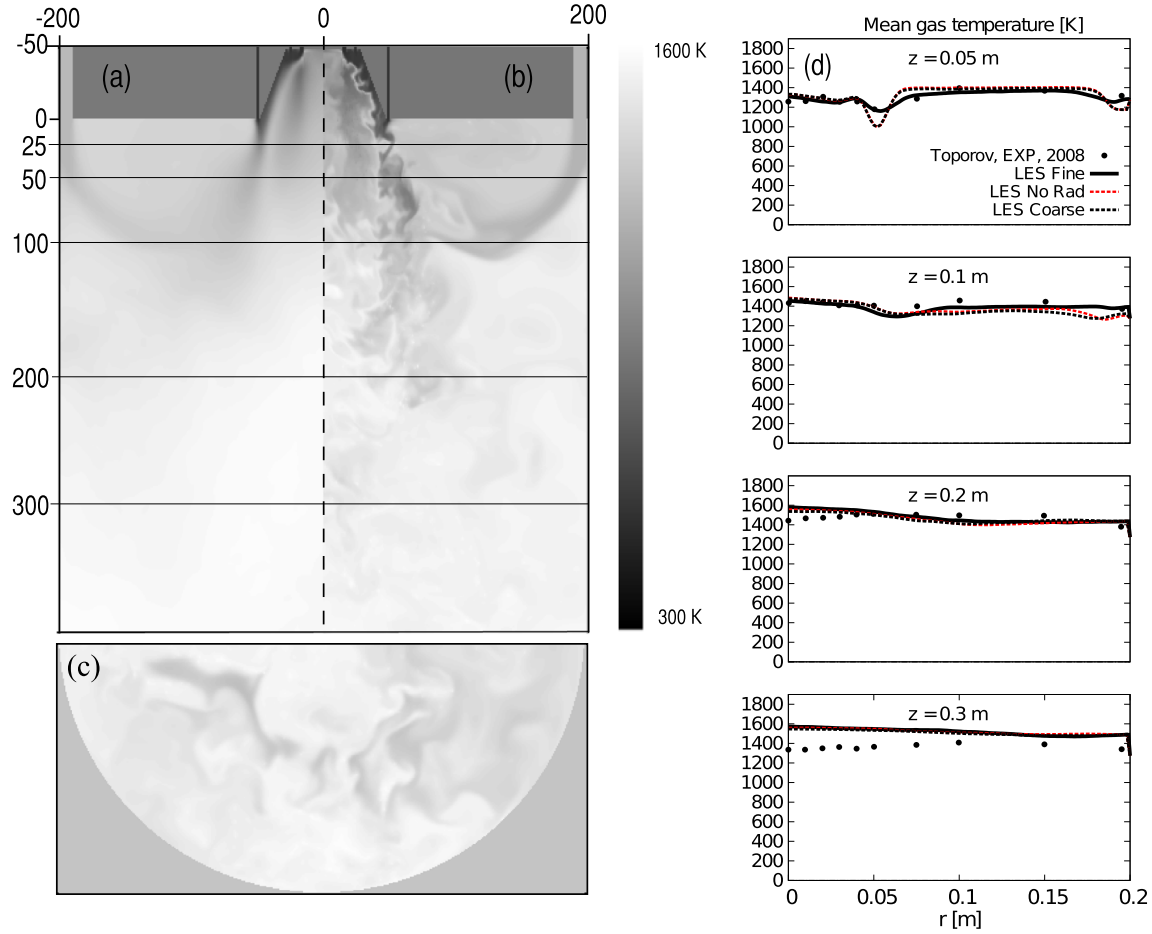

Fig. 10. *Left:* Fine grid LES (a) mean and (b) instantaneous grey scale renderings of gas temperature in a cross-sectional plane along the central axis and (c) cross section of instantaneous gas temperature at $z = 0.35$ m (dimensions are in mm). *Right* (d): Comparison between LES fine (solid line) and coarse with radiation (dotted red line) and without radiation (dotted black line) gas temperature with experimental measurements. (For interpretation of the references to colour in this figure legend, the reader is referred to the web version of this article.)

was artificially diminished by a factor of ten and in another the char combustion was ignored. In the upstream ($z < 0.2$ m) central region of the flame the results with the different char combustion rates show negligible differences. This follows the previous findings, which concluded that in the IRZ and in its surrounding vortex the driving combustion processes are devolatilisation and the burning of the volatile gases.

The results in Section 4 showed that the driving combustion process in the downstream region of the furnace ($z > 0.2$ m) is char combustion. The results observed in Fig. 11 confirm this, indicating a considerable drop in temperature throughout the domain width at the downstream planes when the char combustion rate is diminished. The downstream temperature for the slower char combustion process matches the experimental data at the $z = 0.3$ m plane, which suggests that the current char combustion model over predicts the char combustion rate. A more detailed analysis could involve implementing more advanced char combustion models that account for multiple competing char oxidation reactions [28,46], but it should be stressed that the baseline case presented here was necessary first, before further model improvements can be justified and tested reliably.

5.3. Devolatilisation

To test the effect of the uncertainties in the devolatilisation model, the rate was adjusted. Fig. 11 shows the LES results with the devolatilisation rate constant A_v of Eq. (6) reduced by a factor of ten. In the upstream ($z < 0.2$ m) central region of the flame the results with the slower devolatilisation rate show a large drop in temperature. The previous findings concluded that most of the volatile gases are released and burn within the vortex surrounding the IRZ, leading to the high temperatures observed in the upstream central region of the flame. When the devolatilisation rate is diminished, the particles release most of the volatiles outside the IRZ and burn upstream between $0.05\text{ m} < r < 0.15$ m, producing the high temperatures observed in the same region. The oxygen from the primary and secondary stream is not fully consumed and flows downstream resulting in the higher O_2 concentrations (vol.) and lower temperatures observed throughout the central axis of the furnace.

Fig. 11 shows that the LES results with the slower devolatilisation rate deviate further from the experimental measurements. However, especially in the plane $z = 0.1$ m the temperatures between $0.05\text{ m} < r < 0.15$ m are in closer agreement with the experimental data. This might be attributed to the current devolatilisation model, which does not distinguish between the release of lighter and heavier volatiles. In the experiments the lighter volatiles may be released within the vortex surrounding the IRZ, whilst the heavier tars are released outside. This would have the effect of slightly dropping the high temperatures in the central upstream region of the flame and slightly increasing the temperatures at the sides of the flame between $0.05\text{ m} < r < 0.15$ m, thereby potentially matching more closely the temperature measurements. Ideally, the volatile gases would

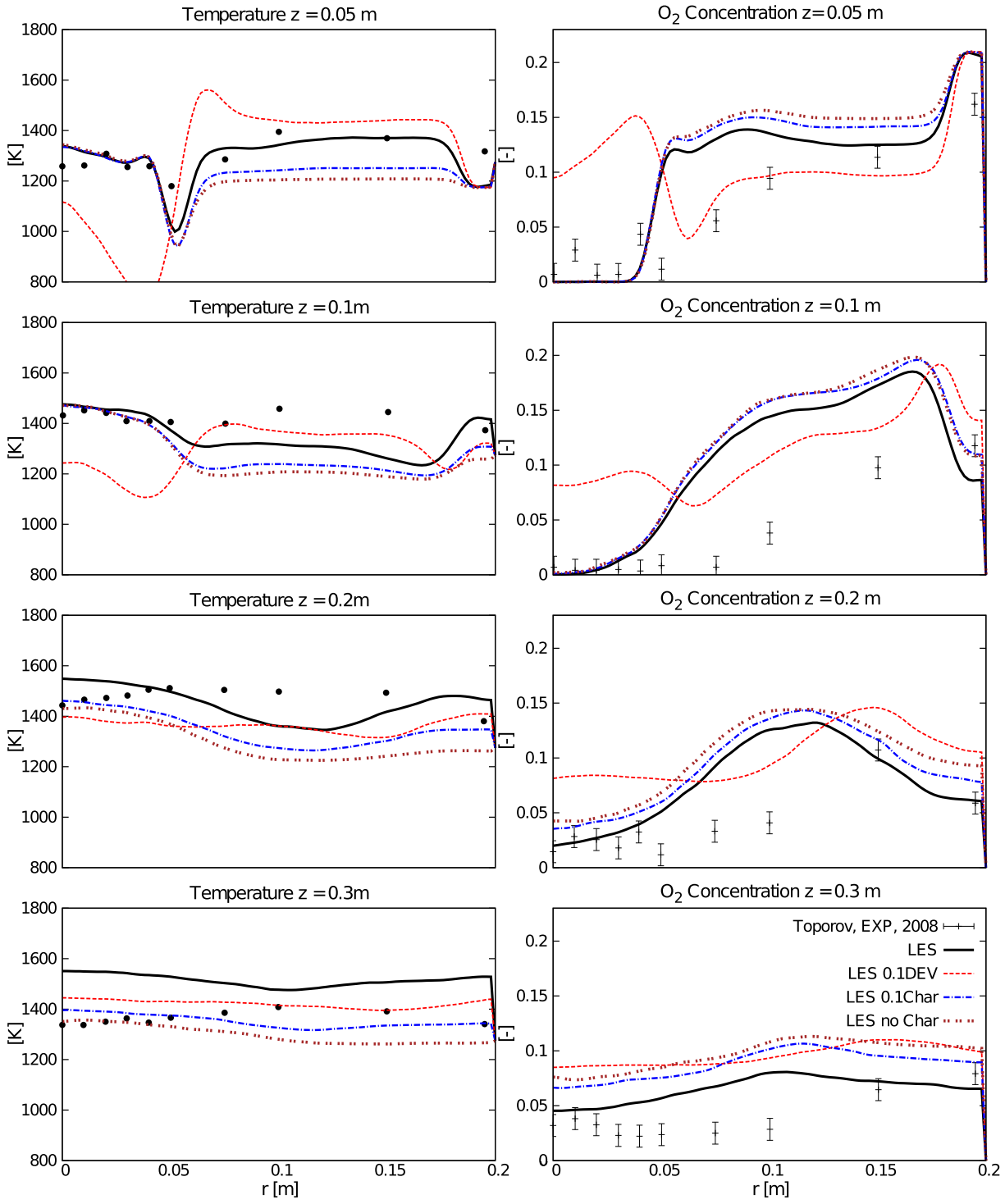

Fig. 11. Comparison between the temperature and oxygen concentrations (vol.) for the slow char combustion, no char combustion and slow devolatilisation.

be represented as light hydrocarbons, tar, carbon dioxide and water vapour, thus removing the need to model them as a single postulated substance. This would allow the use of more advanced devolatilisation models that account for different species and release rates. However, currently transporting multiple species and solving their reactions using multiple reaction chemistry mechanisms, is prohibitively expensive, and could introduce additional uncertainties into the simulation.

6. Conclusions

Large Eddy Simulations were performed of a swirling oxy-coal flame. A working set of LES models for oxy-coal combustion with radiative heat transfer and Lagrangian particle transport have been implemented, tested and verified in comparison to experimental data. A qualitative analysis was made of the flow behaviour in the furnace and the overall PCC processes occurring. The volatiles

are mostly released in the quarl and are burnt rapidly upstream by the O_2 from the primary and secondary streams. Most of the downstream combustion is driven by the char burning with the O_2 from the staging stream. The LES results were compared to experimental data at several locations, showing an overall good agreement in the flame region. A grid resolution study confirmed that almost grid independent results have been obtained. A parametric study was conducted to investigate the effect of the devolatilisation and char combustion rates on the LES results.

Overall, gas-phase temperatures were somewhat over-predicted, but a parameter study revealed an overall sensitivity on the rates of devolatilisation and char combustion. Interestingly, char combustion was found to even affect the recirculation zone near the burner, where one might expect that flame stabilisation and heat release is essentially due to volatile combustion. An interesting problem was observed in predicting the mean velocities, as the experiments have been conducted based on coal particles, so that particle-free outermost stream remained largely invisible to the measurements, but not to the simulations. The current LES was able to predict the flow and combustion, but also provided a wealth of additional time resolved data that can be accessed for further analysis. Such data is particularly relevant for improving boiler performance and for reducing pollutant emissions from flame regions that are not accessible to experimental investigation.

Acknowledgments

The authors gratefully acknowledge the financial support of the Engineering and Physical Science Research Council, and the Center for Computational Science and Simulations (CCSS) of Duisburg-Essen University. We also wish to thank Michele Vascellari of Freiberg University and Oliver Stein of Stuttgart University for many helpful discussions. We also acknowledge funding by DFG through KE-1751/3-1, which supported the conclusion of this work.

References

[1] Backreedy R, Fletcher L, Ma L, Pourkashanian M, Williams A. Modelling pulverised coal combustion using a detailed combustion model. Combust Sci Technol 2006;178:763–87.
[2] Kurose R, Makino H, Suzuki A. Numerical analysis of pulverized coal combustion characteristics using advanced low-NOx burner. Fuel 2004;83:693–703.
[3] Lockwood FC, Salooja AP. The prediction of some pulverized bituminous coal flames in a furnace. Combust Flame 1983;54:23–32.
[4] Kurose R, Makino H. Large eddy simulation of a solid fuel jet flame. Combust Flame 2003;135:1–16.
[5] Yamamoto K, Murota T, Ozkazaki T, Taniguchi M. Large eddy simulation of a pulverized coal jet flame ignited by a preheated gas flow. Proc Combust Inst 2011;33:1771–8.
[6] Edge P, Gubba S, Ma L, Porter R, Pourkashanian M, Williams A. LES modelling of air and oxy-fuel pulverised coal combustion – impact on flame properties. Proc Combust Inst 2011;33:2709–16.
[7] Gharebaghi M, Irons R, Ma L, Pourkashanian M, Pranzitelli A. Large eddy simulation of oxy-coal combustion in an industrial combustion test facility. Int J Green Gas Control 2011;55:100–10.
[8] Franchetti B, Marincola FC, Navarro-Martinez S, Kempf AM. Large eddy simulation of a pulverised coal jet flame. Proc Combust Inst 2013;34:2419–26.
[9] Stein O, Olenik G, Kronenburg A, Cavallo-Marincola F, Franchetti B, Kempf A, Ghiani M, Vascellari M, Hasse C. Towards comprehensive coal combustion modeling for LES. Flow Turbul Combust 2013;90(4):859–84.
[10] Pedel J, Thornock J, Smith P. Large eddy simulation of pulverized coal jet flame ignition using the direct quadrature method of moments. Energy Fuels 2012;26(11):6686–94.
[11] Rabacal M, Franchetti B, Marincola FC, Proch F, Costa M, Hasse C, et al. Large eddy simulation of coal combustion in a large scale laboratory furnace. Proc Combust Inst 2015;35(3):3609–17.
[12] Pedel J, Thornock JN, Smith PJ. Ignition of co-axial turbulent diffusion oxy-coal jet flames: experiments and simulations collaboration. Combust Flame 2013;160:1112–28.
[13] Heil P, Toporov D, Stadler H, Tschunko S, Forster M, Kneer R. Development of an oxycoal swirl burner operating at low O_2 concentrations. Fuel 2009;88:1269–74.
[14] Toporov D, Bocian P, Heil O, Kellermann A, Stadler H, Tschunkoschunko S, et al. Detailed investigation of a pulverised fuel swirl flame in CO_2/O_2 atmosphere. Combust Flame 2008;155:605–18.
[15] Vascellari M, Locci C, Cau G. Influence of turbulence–chemical interaction on modelling of a pulverised coal oxycombustion flame operating at low O_2 concentrations. In: ASME-ATI-UIT conference on thermal and environmental issues in energy systems.
[16] Chen L, Ghoniem AF. Simulation of oxy-coal combustion in a 100 kWth test facility using RANS and LES: a validation study. Energy Fuels 2012;26:4783–98.
[17] Kempf A, Geurts B, Oefelein J. Error analysis of large-eddy simulation of the turbulent non-premixed Sydney bluff-body flame. Combust Flame 2011;158:2408–19.
[18] Cavallo-Marincola F, Ma T, Kempf A. Large eddy simulations of the Darmstadt turbulent stratified flame series. Proc Combust Inst 2013;34(1):1307–15.
[19] Rittler A, Proch F, Kempf AM. LES of the Sydney piloted spray flame series with the PFGM/ATF approach and different sub-filter models. Combust Flame 2015;164(4):1575–98.
[20] Smagorinsky J. General circulation experiments with the primitive equations – the basic experiments. Month Weather Rev 1963;91:99–164.
[21] Jones W, Lyra S, Navarro-Martinez S. Large eddy simulation of a swirl stabilized spray flame. Proc Combust Inst 2011;33:2153–60.
[22] Bini M, Jones W. Large eddy simulation of particle-laden flows. J Fluid Mech 2008;614:207–52.
[23] Yuen M, Chen L. On drag of evaporating liquid droplets. Combust Sci Technol 1976;21:537–42.
[24] Lyra S. Large eddy simulation of isothermal and reacting sprays. London: Imperial College; 2010 [PhD thesis].
[25] Ranz W, Marshall W. Evaporation from drops, part 1. Chem Eng Prog 1952;48:141–6.
[26] Franchetti B. Large eddy simulation of air and oxy-coal combustion. London: Imperial College; 2014. PhD thesis.
[27] Edge P, Gharebaghi M, Irons R, Porter R, Porter R, Pourkashanian M, et al. Combustion modelling opportunities and challenges for oxy-coal carbon capture technology. Chem Eng Res Des 2011;89:1470–93.
[28] Shaddix CR, Molina A. Particle imaging of ignition and devolatilization of pulverized coal during oxy-fuel combustion. Proc Combust Inst 2009;32:2091–8.
[29] Badzioch S, Hawksley P. Kinetics of thermal decomposition of pulverized coal combustion. Ind Eng Chem Process Des Develop 1970;9:521–30.
[30] Fletcher T, Kerstein A, Pugmire R, Solum M, Grant D. Chemical percolation model for devolatilization. 3. Direct use of carbon-13 NMR data to predict effects of coal type. Energy Fuels 1992;6(4):414–31.
[31] Genetti D, Fletcher T, Pugmire R. Development and application of a correlation of C-13 NMR chemical structural analyses of coal based on elemental composition and volatile matter content. Energy Fuels 1999;13(1):60–8.
[32] Baum M, Street P. Predicting the combustion behaviour of coal particles. Combust Sci Technol 1971;3:231–43.
[33] Field M. Rate of combustion of size-graded fractions of char from low-rank coal between 1200 K and 2000 K. Combust Flame 1969;13:237–52.
[34] Smoot L, Pratt D. Pulverised-coal combustion and gasification. Theory and applications for continuous flow processes. New York: Plenum; 1979.
[35] Spalding DB. Development of the eddy-break-up model of turbulent combustion. Proc Combust Inst 1977;16(1):1657–63.
[36] Zhou L, Hu L, Wang F. Large-eddy simulation of turbulent combustion using different combustion models. Fuel 2008;87:3123–31.
[37] Truelove J. Discrete-ordinate solutions of the radiation transport equation. ASME J Heat Transf 1987;109:1048–51.
[38] Chandrasekhar S. Radiative transfer. New York: Dover Publications; 1960.
[39] Fiveland W. Three-dimensional radiative heat-transfer solutions by the discrete-ordinates method. J Thermophys Heat Transf 1988;2(4):309–16.
[40] Gosman AD, Lockwood FC. Incorporation of a flux model for radiation into a finite-difference procedure for furnace calculations. Proc Combust Inst 1973;14(1):661–71.
[41] Chui EH, Hughes PMJ, Raithby GD. Implementation of the finite volume method for calculating radiative transfer in a pulverized fuel flame. Combust Sci Technol 1993;92:225–42.
[42] Kempf A, Klein M, Janicka J. Efficient generation of initial and inflow conditions for transient turbulent flows in arbitrary geometries. Flow Turbul Combust 2005;74:67–84.
[43] Pettit M, Coriton B, Gomez A, Kempf A. Large eddy simulation and experiments on non-premixed highly turbulent opposed jet flows. Proc Combust Inst 2011;33:1391–9.
[44] Cavallo-Marincola F. Large eddy simulation of pulverised coal combustion. London: Imperial College; 2014. PhD thesis.
[45] Michel JB, Payne R. Detailed measurements of long pulverized coal flames for the characterization of pollutant formation. Technical report, International Flame Research Foundation.
[46] Hecht ES, Shaddix CR, Lighty JS. Analysis of the errors associated with typical pulverized coal char combustion modeling assumptions for oxy-fuel combustion. Combust Flame 2013;160(8):1499–509.